Journal of Advanced Joining Processes 12 (2025) 100365

Contents lists available at ScienceDirect

Journal of Advanced Joining Processes

journal homepage: www.sciencedirect.com/journal/journal-of-advanced-joining-processes

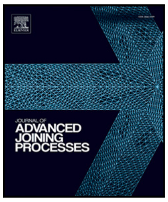

Analysis of precipitation kinetics during refill friction stir spot welding and post-weld heat treatments in AA7050 using SAXS and numerical modeling

Susanne Henninger [a,*], Rupesh Chafle [b], Niklaas Becker [b], Camila C. de Castro [b,c], Benjamin Klusemann [b,c], Martin Müller [a], Peter Staron [a]

[a] Helmholtz-Zentrum Hereon, Institute of Materials Physics, Max–Planck-Straße 1, 21502 Geesthacht, Germany
[b] Helmholtz-Zentrum Hereon, Institute of Material and Process Design, Max–Planck-Straße 1, 21502 Geesthacht, Germany
[c] Leuphana University Lüneburg, Institute for Production Technology and Systems, Universitätsallee 1, 21335, Lüneburg, Germany

ARTICLE INFO

Keywords:
Aluminum alloy
Refill friction stir spot welding
Post-weld heat treatment
Precipitation kinetics
Modeling

ABSTRACT

The impact of the refill friction stir spot welding process (refill FSSW) on precipitates in a high-strength AA7050-T7651 alloy is studied. Cross-sections of the welded samples are analyzed via small-angle X-ray scattering (SAXS), yielding 2D maps of spatial distributions of precipitate volume fraction and mean radius. The welding plunge times are varied during refill FSSW, leading to an increase in the width of the heat-affected zone (HAZ) with increase in energy input. The mean radius of precipitates increases above 25 nm at the edges of the stir zone (SZ) and thermo-mechanically affected zone (TMAZ). Dissolution and growth of η-precipitates in the HAZ are measured in-situ and are successfully modeled with the PanPrecipitation software. Moreover, the effect of various post-weld heat treatments (PWHT) on the precipitate distribution in the weld is analyzed. Reprecipitation in the HAZ is seen already after short aging times. After 20 min, the volume fraction increases all over the HAZ and nearly reaches the volume fraction of the base material. In the SZ/TMAZ, GP zones are formed through natural aging after welding and the PWHT lead to phase transformations and an increase in volume fraction and precipitate growth. Precipitates grow to a size of 2.5 nm after PWHT at 120 °C and 6.5 nm at 163 °C. Thus, the formation of $\eta' + \eta$-phase is expected after PWHT. Hardness measurements show that the PWHT lead to a hardness increase in the SZ and outer HAZ, but a minimum remains in the TMAZ/HAZ, where precipitates coarsened during welding. No significant changes in the weld zone features and the corresponding microstructure are observed between the as-welded and PWHT joints, indicating that the time–temperature conditions do not induce transformations such as grain growth and/or static recrystallization.

Introduction

According to the market predictions of the two largest aircraft companies, Airbus and Boeing, a huge growth in the aviation industry is expected for the period 2024–2043 (Airbus, 2024; Boeing, 2024). While around 25,000 airplanes were in operation in 2023, a fleet size of around 50,000 airplanes is predicted for the year 2043. As the current fleet is also aging, a delivery of around 42,000 airplanes is expected in this period and additionally, ambitious climate goals need to be achieved (Airbus, 2024; Boeing, 2024). For further de-carbonization of aviation, new technologies and alloys have to be developed, where lightweight design is an important factor as additional weight reductions lead to an increased range and less fuel consumption Dursun and Soutis (2014), Zhou et al. (2021).

High-strength AA7xxx alloys (Al–Zn–Mg–Cu) are widely used in the aviation industry, e.g. for the fuselage and wing skins. These alloys show a high strength-to-weight ratio, high toughness, good workability and corrosion resistance (Azarniya et al., 2019; Zhou et al., 2021). The 7xxx series is heat-treatable and hence, precipitation hardening is the main strengthening mechanism. Through a solution treatment, quenching and age hardening procedure, precipitates of a second phase are formed inside the Al matrix. The type, geometry and density of these precipitates determine the mechanical properties of these alloys (Azarniya et al., 2019), which makes it so important to understand their precipitation kinetics in detail. The typical precipitation sequence of AA7xxx alloys is as follows (Heidarzadeh et al., 2021; Cao et al., 2019): supersaturated solid solution (SSSS) → GP zones → η' → η ($MgZn_2$). Through variations in the artificial aging procedure, the precipitate phase as well as their size, volume fraction and density can be tailored. For a better corrosion resistance, these alloys are often used in an overaged T7 condition (Azarniya et al., 2019; Zhou et al., 2021).

---

[*] Corresponding author.
E-mail address: susanne.henninger@hereon.de (S. Henninger).

https://doi.org/10.1016/j.jajp.2025.100365
Received 6 June 2025; Received in revised form 21 November 2025; Accepted 27 November 2025

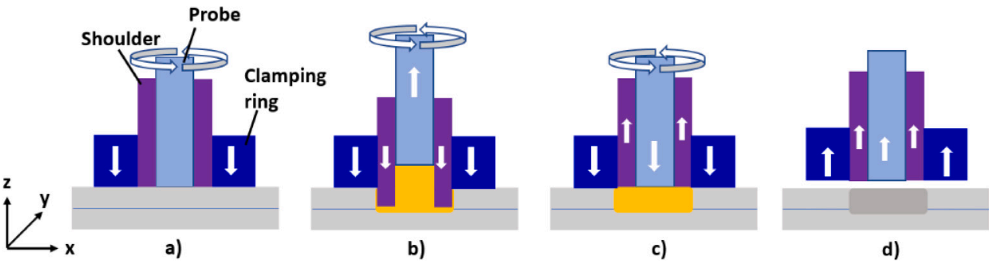

Fig. 1. Schematic setup and principle of refill FSSW in the shoulder plunge variant.

Several AA7xxx alloys (AA7449, AA7475, AA7050) were studied in an overaged state and mostly η-precipitates with small amounts of η' were found (De Geuser and Deschamps, 2012; Dumont et al., 2006; Fribourg et al., 2011; Gao et al., 2024; Jacumasso et al., 2016).

These alloys have the disadvantage that their weldability is low due to weld cracking or distortion (Dursun and Soutis, 2014). Therefore, riveting is the traditional joining technique for 7xxx alloys in fuselage and wing structures. However, riveting requires several processing steps and rivets lead to an increase in weight. Furthermore, it can cause fatigue cracking due to stress concentrations (Zhou et al., 2021), but in contrast, riveting can also lead to a longer fatigue life as the crack can be stopped when it grows into the rivet hole (Zhang et al., 2022). Solid-state joining techniques offer the possibility of joining alloys which are regarded as conventionally non-weldable, such as 7xxx alloys. As the materials are joined below the melting point, defects such as porosity and hot cracking can be avoided (Dursun and Soutis, 2014). Refill friction stir spot welding (refill FSSW) is a solid-state process with a high potential to replace single-spot joining methods such as riveting or resistance spot welding in the automotive and aerospace industries and thus, leading to weight reductions (Shen et al., 2020; Meng et al., 2021). Additionally, it can be used for exit hole closure (Reimann et al., 2017) or repairing of fatigue cracks (Shen et al., 2020).

Refill FSSW is based on the principle of friction stir welding (FSW), but without the lateral movement of the tool. The process in the shoulder plunge variant is schematically shown in Fig. 1. In the first step, Fig. 1(a), the stationary clamping ring ensures that the sheets are firmly fixated to the backing plate, while shoulder and probe start rotating in the same direction at the same rotational speed. As soon as the rotating tool comes in contact with the material, Fig. 1(b), frictional heat is created and the material plastically deforms. In this variant, the shoulder plunges into the material while the probe moves in the opposite direction. The material is plasticized and flows into the cavity created by the probe. In the third step, Fig. 1(c), the movement of probe and shoulder is reversed and the plasticized material is filling the previous cavity within the sheets. Finally, the tool stops rotating, retracts and a weld without exit hole is obtained, Fig. 1(d). Important process parameters are the tool rotational speed, plunge time and plunge depth. Additionally, a dwell time can be added for a certain duration between plunging and retracting of the tool, which improves mixing and bonding of the sheet materials. However, in precipitation hardened Al alloys this might lead to a broader softened region. Dwell times are especially interesting for metals with a higher melting point (Shen et al., 2020). The development of numerical models makes it possible to investigate the thermo-mechanical and material flow during the process in more detail. For instance, Janga et al. (2025) developed a smoothed-particle hydrodynamics model (SPH) that modeled the refill FSSW process for AA7075-T6, where predicted temperature curves corresponded to experimentally measured temperatures. Thus, the impact of varying welding parameters on temperature evolution can be studied. Another prominent modeling technique is the finite element approach that can also be used to model the temperature distribution, which can be used to predict the microstructure evolution at the welding interface during refill FSSW (Raza et al., 2022). Due to the high strain rates and temperatures, the microstructure during refill FSSW is affected similar to the FSW process, so that stir zone (SZ), thermo-mechanically affected zone (TMAZ) and heat-affected zone (HAZ) can be identified after refill FSSW. Precipitates are affected by plastic deformation as well as heat, i.e. dissolution and coarsening of precipitates can be observed, leading to softening of the material especially in the HAZ, where typically the hardness minimum is found (Shen et al., 2020; Meng et al., 2021; Bush et al., 2024; Reynolds et al., 2005).

Different strategies are developed to improve the joint quality, such as ultrasonic assisted (Guo et al., 2023) or submerged FSW (Rathinasuriyan et al., 2021). Additionally, process modification strategies or post-processing strategies can be used (Habba and Ahmed, 2025). Furthermore, through the application of post-weld heat treatments (PWHT), the weakened welding zones can be strengthened again. The effects of natural aging as well as artificial aging after FSW of AA7xxx were studied in literature, but ambivalent results were obtained. While some authors observed negative or no influence of the applied PWHT to some welding zones, especially the HAZ (Sullivan and Robson, 2008; Reynolds et al., 2005), in other works positive responses were obtained (Kumar et al., 2015; Fuller et al., 2010; Gupta et al., 2022; Lezaack and Simar, 2021). A review of the influence of PWHT on FSW Al samples is given by Maji et al. (2021). Various parameters can influence the material behavior during PWHT, which are discussed hereafter. Compositions and tempers of the base material varied, making direct comparisons between literature data difficult. Additionally, aging treatments were conducted with variations in aging temperatures and durations. Some samples were artificially aged, others naturally aged at room temperature. Some aging treatments were conducted with solution heat treatment before the artificial aging step, while others skipped the solution treatment (Dong et al., 2023). A solution treatment at 480 °C, followed by artificial aging at 120 °C can lead to a homogeneous hardness distribution all over the welding zones, e.g. Sivaraj et al. (2014). However, the solution heat treatment can also cause secondary recrystallization or abnormal grain growth, which is detrimental for mechanical properties (Lezaack and Simar, 2021). Another important parameter is the thermal history of the material during welding. Through different peak temperatures or heating and cooling rates, the solute concentration after welding varies, which influences the ability of reprecipitation (Reynolds et al., 2005; Bush et al., 2024). This shows the importance of analyzing precipitation kinetics during welding as well as during PWHT in more detail. Small-angle X-ray scattering (SAXS) gives the opportunity to study the evolution of particle size distributions during ex-situ and in-situ measurements. Combined with numerical modeling, a deep understanding of kinetics can be obtained. In a previous work (Henninger et al., 2025), we calibrated a Pandat model using reversion experiments of AA7050. Further, we were able to successfully model the influence of time–temperature cycles, which occur in the HAZ during FSW, on precipitates in AA7050. However, during refill FSSW the welding times are significantly shorter compared to FSW, the maximum temperatures in the SZ are higher and higher heating and cooling rates are obtained (Shen et al., 2020).

In this work, the influence of plunge time during refill FSSW on precipitation kinetics in AA7050 was studied with SAXS mapping after welding. The influence of time–temperature curves, which were

Table 1
Welding parameters used during refill FSSW on AA7050-T7651 samples.

Sample	Plunge depth [mm]	Rotational speed [rpm]	Plunge time [s]	Plunging speed [mm/s]
Fast	2.6	2700	1.5	1.75
Medium	2.6	2700	2.1	1.25
Slow	2.6	2700	3.5	0.75

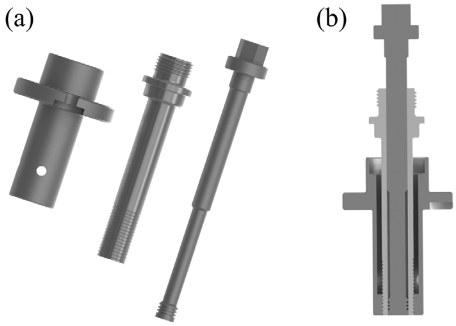

Fig. 2. Refill FSSW tool: (a) clamping ring, shoulder and probe (from left to right), and (b) cross-sectional view of tool assembly.

measured at different locations during the welding process, was simulated during in-situ SAXS measurements with a dilatometer. These heat treatments were also modeled using the developed Pandat model, and it is shown that it can successfully describe the kinetics in the HAZ during refill FSSW. Finally, different PWHT were performed and additionally the impact of the duration of the PWHT was analyzed with 2D SAXS mapping. Thus, this work shows for the first time the influence of welding parameters during refill FSSW and heat treatments after welding on the precipitate distribution at a high spatial resolution. In addition, the precipitation modeling provides detailed insights into precipitation kinetics. The combination of unique data and numerical modeling improves the understanding of the refill FSSW process in detail.

Experimental and modeling methods

Variation of plunge time during refill FSSW

For the analysis of precipitation kinetics during refill FSSW, AA7050 samples in the overaged condition T7651 were used. Typical mechanical properties of that material are a yield strength of 490 MPa, ultimate tensile strength of 552 MPa and an elongation at break of 11% (Barbini et al., 2018; Wu et al., 2015). For simplification of the analysis of precipitation kinetics, spots were welded only into one sheet instead of the typical overlap configuration, involving two sheets. The Al samples had a size of 125 mm × 125 mm and a thickness of 5.2 mm.

The RPS100 machine from Harms & Wende (Germany) was used for the refill FSSW process, where the probe had a diameter of 6 mm, the shoulder a diameter of 9 mm and the clamping ring a diameter of 17 mm, as illustrated in Fig. 2. A clamping force of 16 kN was used during all experiments. Plunge depth and rotational speed were kept constant, while the plunging speed was varied, leading to different plunge times. No dwell time was added. The parameters are described in detail in Table 1. With the variation of plunge time, the influence of heat input on precipitation kinetics could be studied, as it is a function of welding time. Plunge depth was chosen based on previous results (Becker et al., 2024). The selected rotational speed of 2700 rpm leads to defect-free welds for the range of plunge speed that was used.

Temperature measurements were conducted during each welding process using K-type thermocouples. As it is not possible to measure temperatures directly within the SZ, measurements were conducted 0.5 mm away from the lower edge of the sample at three different distances from the welding center. It was measured in the center of the spot weld (x = 0 mm), at x = 6.5 mm and x = 11.5 mm. The respective time–temperature curves for the three weldings measured at the three positions are shown in Fig. 3.

To study the influence of plunge time on the microstructure in more detail, cross-sections of the welded sheets were analyzed via SAXS. Hence, samples with the dimensions x = 125 mm, y = 2 mm and z = 5.2 mm were eroded in the center of the welded spots parallel to the rolling direction, see Fig. 4(a). The SAXS measurements were carried out 75 days after welding and thus, natural aging is expected.

Conducted post-weld heat treatments

Additional samples with the parameters in Table 1 were welded and different PWHT were conducted. Three sheets were welded of each parameter set and samples were eroded as described above. 20 days after welding, these samples were heat-treated using a forced convection chamber furnace (model NA 120/851 by Nabertherm GmbH, Germany). Different industrial relevant heat treatments were conducted, which are described in detail in Table 2. HT 3 was conducted at 120 °C, which leads to a peak-aged condition. HT 1 and HT 2 were conducted at 163 °C, with a two-step aging in HT 1, both leading to an overaged state. No solution heat treatment was done before artificial aging, as abnormal grain growth should be avoided. SAXS measurements were conducted 4–8 days after the PWHT.

To study the influence of the duration of PWHT in more detail, samples were heat treated at 163 °C for various times, see HT 4. Five sheets were welded with the slow welding process, samples were eroded and heat treated 22 days after welding. For comparison, one sample was analyzed in the as-welded state. The other four samples were heated to a temperature of 163 °C with a heating rate of 30 °C/h and held at that temperature for different durations. The first sample was taken out and water quenched after 20 min, the others after 1 h, 3 h and 9 h, respectively. 5–7 days after the PWHT the samples were analyzed via 2D SAXS mapping.

Microstructure analysis of the welds and microhardness measurements

The microstructures of an as-welded sample and three heat-treated samples (120 °C for 24 h, 163 °C for 20 min and 9 h) were studied. Microstructural analysis of welds cross-sections was performed using an optical microscope (DMi8, Leica, Germany) under polarized light. For this purpose, the samples were cut, embedded in acrylic resin and prepared according to standard metallographic procedures, which consisted of grinding and polishing the surfaces up to a finish with colloidal silica suspension. The polished specimens were then electrolytically etched using Barker's reagent. The grain sizes of the resulting micrographs were determined using the linear intercept method. After the microstructural investigation, the polished specimens were subjected to microhardness measurements using an automated testing machine (Durascan 70 G5, EMCO-TEST Prüfmaschinen) in accordance with DIN EN ISO 6508-1. In order to obtain microhardness maps, measurements were performed at intervals of 0.25 mm between indentations along the x- and z-directions, using a load of 0.2 kg at a holding time of 10 s and a Vickers indenter with an opening angle of 136°.

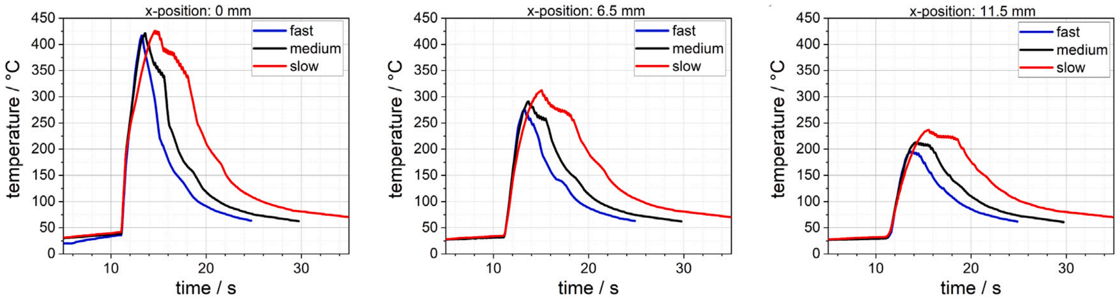

(a) (b) (c)

Fig. 3. Measured temperature profiles during refill FSSW 0.5 mm away from the lower sample edge and different distances to the welding center: (a) x = 0 mm, (b) x = 6.5 mm and (c) x = 11.5 mm. The position of the thermocouples is schematically shown in Fig. 4(a).

Table 2
Conducted PWHT after the refill FSSW process on AA7050-T7651 samples.

Heat treatment	Aging temperature and duration
HT 1	120 °C for 5 h (heating rate: 30 °C/h) + 163 °C for 12 h (heating rate: 15 °C/h), quenching
HT 2	163 °C for 12.5 h (heating rate: 30 °C/h), quenching
HT 3	120 °C for 24 h (heating rate: 30 °C/h), quenching
HT 4	163 °C (heating rate: 30 °C/h) for various times: 20 min, 1 h, 3 h and 9 h, quenching

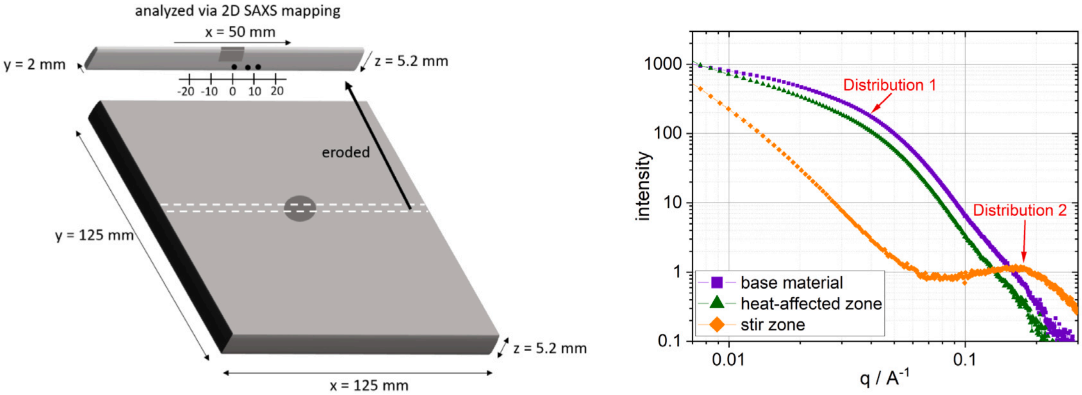

(a) (b)

Fig. 4. (a) Schematic setup of a spot welded AA7050 sheet and an eroded sample used for 2D SAXS mapping. The black dots indicate the position of the thermocouples in the full substrate material. (b) Exemplary SAXS scattering curves measured at the cross-section of a welded sample. In the SZ, a second size distribution was used for fitting.

SAXS measurements

The beamline P07, which is run by Helmholtz-Zentrum Hereon at Deutsches Elektronen-Synchrotron (DESY), Germany, was used for the implementation of both ex-situ and in-situ SAXS measurements. High photon energies of 73 keV, which correspond to a wavelength of 0.17 Å, were used to penetrate the Al samples.

The cross-sections of the three samples, which were welded with different plunge times, were analyzed with 2D SAXS mapping and thus, a thickness of 2 mm was irradiated. Within the sheet planes, a length of x = 50 mm was mapped with a resolution of 0.5 mm. The middle of the welded spot was defined as x = 0, see Fig. 4(a). In sheet thickness direction, 8 lines were scanned with a resolution of 0.6 mm, leading to 808 points per sample. The nine heat-treated samples (HT 1-3) were mapped in the same way, but only 40 mm were measured within the sheet plane with a resolution of 0.5 mm and only 5 rows with a resolution of 1.22 mm were scanned in thickness direction, leading to 405 points per sample. All samples were measured with an exposure time of 5 s. A Varex XRD 4343 detector with a pixel size of 150 μm × 150 μm and total number of 2880 × 2880 pixels was used for these experiments. Finally, the five samples which were heat treated for various times (HT 4), were measured with a PILATUS3 X CdTe 2M detector. This detector is constructed out of 3 × 8 detector modules. The size of the pixels is 172 μm × 172 μm and it has a total number of 1475 × 1679 pixels. 40 mm of these samples were scanned within the sheet planes with a resolution of 0.5 mm and 9 rows were measured in thickness direction with a resolution of 0.6 mm. An exposure time of 0.2 s was used for these measurements. During the ex-situ 2D scans the distance between detector and sample came to 11.9–12.3 m, varying slightly between the different beamtimes. The beam had a cross-section of 0.2 mm × 0.2 mm.

Additionally, in-situ heat treatments were conducted using a modified dilatometer DIL 805A/D (TA Instruments) at the beamline P07. For these experiments, hollow cylindrical samples with a length of 10 mm, diameter of 4 mm and a wall thickness of 0.8 mm were fabricated from the AA7050-T7651 sheet material. Hence, a total thickness of 1.6 mm was irradiated. S-type thermocouples were spot welded onto the surface of the samples to precisely measure and control the applied temperature. With the dilatometer it is possible to study the influence of temperature on precipitation kinetics in high temporal resolution. Thus, to obtain more information about the influence of temperature during refill FSSW, the time–temperature curves that were measured during the welding process at 6.5 mm and 11.5 mm, see Fig. 3(b) and (c), were simulated in the dilatometer. The exposure time was set to 0.2 s and the PILATUS3 X CdTe 2M detector was used. Through the usage of the dilatometer, the distance between detector and sample was slightly smaller at around 10.5 m.

For calibration of the setup during all experiments, silver behenate was used to get the correct sample-detector distance. Glassy carbon was used for calibration of the macroscopic scattering cross-section. A tungsten beam stop with a diameter of 0.2 mm was used for protection of the detector. The beam stop as well as dead pixels were masked before integration. A transmission of 86% was measured for the 2 mm thick ex-situ samples and 88% for the 1.6 mm thick in-situ samples. With the Nika-software (Ilavsky, 2012) the SAXS signal was azimuthally integrated, subtracting the background. The measured q-range was 0.007–0.3 A^{-1}. After integration, the Irena-software (Ilavsky and Jemian, 2009) was used for fitting and further analysis. As the AA7050 base material was in an overaged T7651 state, the expected main precipitate phase was the equilibrium η-phase with small amounts of η', which was neglected in this work. A composition of $MgZn_2$ and a density of 5.09 g/cm^3 (Villars, 2023) was assumed for the precipitates, leading to a scattering contrast $(\Delta\rho)^2$ of $3.25 \cdot 10^{22}$ cm^{-4} between Al matrix and precipitates. The composition and therefore scattering contrast was assumed to be constant during all experiments. It is known, however, that the precipitate composition can change with time at elevated temperatures and that not only Mg and Zn, but also Cu and Al can be present within the precipitates. Methods like, e.g., atom probe tomography are required to determine the composition of nano-precipitates (Marlaud et al., 2010b). The precipitate volume fraction in the AA7050-T7651 base material derived from the SAXS measurements assuming $MgZn_2$ precipitates, f_{max}, equals to 3.8%. η-precipitates were fitted using a lognormal size distribution (distribution 1), where a spheroidal shape with an aspect ratio of 0.4 was assumed (Marlaud et al., 2010a). Liu et al. analyzed the influence of chemical composition (Liu et al., 2015) as well as the influence of temper condition (Liu et al., 2013) in AA7xxx alloys via SAXS and fitted the aspect ratio in the range of 0.4–0.6 in all sample, which validates our assumption.

In Fig. 4(b) three exemplary SAXS scattering curves are shown, measured at different positions during the 2D SAXS scan. The variation between the welding zones can be clearly seen. Compared to the base material, the intensity decreases in the HAZ. In the SZ, intensity at low q decreases even more, but a shoulder at around 0.2 A^{-1} emerges. This shows that a second size distribution is necessary for covering very small precipitates. Hence, distribution 2 describes small GP zones, which form through natural aging after welding. Again, a lognormal size distribution was used. As it is very difficult to obtain information about these small precipitates (1–2 nm), a spheroidal shape with an aspect ratio of 0.4 and a constant composition of $MgZn_2$ was assumed for these precipitates. The standard deviation of the size distribution was fixed to a value of 0.2. As these precipitates were so small and occurred with a high number density, interaction between the scattering from neighboring particles was taken into account and hence, the InterPrecipitate model within Irena was used as structure factor. The function used in this model is based on the interaction between precipitates in nickel-based superalloys (Huang et al., 2008), but it has already been successfully used for precipitates in Al–Mg–Zn–Cu alloys (Liu et al., 2015, 2013) and seemed suitable for this work. With the application of PWHT, these GP zones in the SZ/TMAZ dissolve or might transform into η' or η-precipitates. Hence, after PWHT distribution 2 described η'+η-precipitates, where no interaction parameter was necessary anymore and standard deviation was a free fitting parameter, whereas shape and composition of distribution 2 stayed constant. During all experiments, precipitates which were already present in the base material, were fitted by distribution 1.

Table 3

Parameters used for the Pandat simulations. Calibration was conducted in previous work using reversion experiments (Henninger et al., 2025).

Parameter	Value	Unit
Molar Volume (Al)	$1.0425 \cdot 10^{-5}$ (CompuTherm LLC, 2021)	m^3/mol
Molar Volume (η)	$1.015 \cdot 10^{-5}$ (Kammerer et al., 2015)	m^3/mol
Interfacial Energy (Al-η)	0.12	J/m^2
Effective Diffusivity Factor	1	–
Kinetic Parameter Factor	3	–

Modeling of precipitation kinetics with a calibrated Pandat model

The commercial Pandat software (CompuTherm LLC, 2025), which is developed by CompuTherm LLC, was used to model precipitation kinetics in AA7050. The Pandat version 2021 with the PanAl TH+MB database has been used. Details on the functionality and applied models within Pandat can be found elsewhere (Cao et al., 2009). The employed Pandat model was calibrated using reversion experiments on AA7050 in a previous work (Henninger et al., 2025). Therefore, this model was used to simulate precipitation kinetics in the HAZ during refill FSSW in this work, where fast heating and cooling rates dominate precipitation kinetics. The time–temperature curves shown in Fig. 3(b) and (c) were simulated with this model, corresponding to the conditions in the in-situ dilatometer tests as described above.

The Pandat model was calibrated on an AA7050-T7451 alloy and was used for the studied AA7050-T7651 alloy in this work as well. The composition of AA7050 alloys has to lie within a narrowly defined range (European Committee for Standardization - E.N. 573-3, 2024) and hence, no huge discrepancy in precipitation kinetics is expected through slight composition variations between the studied sheet materials. The alloy was treated as a ternary Al-6.41 Zn-2.03 Mg (in wt.%) alloy and only η-precipitates with the fixed composition $MgZn_2$ in an Al matrix were considered. As the alloy was used in an overaged state, it was assumed to be close to equilibrium condition. An equilibrium volume fraction of f_{max}=4.5% η-phase was calculated using the Pandat thermodynamic database. The difference between f_{max} derived from the Pandat database and from the SAXS measurements could be due to the unknown chemical composition of the precipitates. However, the influence on the general characteristics of the precipitation kinetics should be small. As precipitates were present in the base material, the corresponding starting size distribution was defined. A lognormal size distribution with a standard deviation of 0.4, volume fraction of 4.5% and a mean radius of 6.4 nm was used. For the calculation of the kinetics, a Kampmann-Wagner model with 100 size classes was used in PanPrecipitate. Although from SAXS experiments the mean radius was calculated as average of the particle volume distribution, Pandat calculated it as average of the particle number density distribution. Hence, a recalculation from number to volumetric mean radii with an aspect ratio of 0.4 was done. The used parameters for the Pandat model are provided in Table 3.

Predictions for further time–temperature curves were made. For that purpose, the temperature curve, which was measured during the medium speed welding process at x = 6.5 mm, see Fig. 3(b), was taken as master curve. To see the influence of faster and slower plunging speeds, the time scale was multiplied with prefactors of 0.25, 0.5, 2 and 4, and resulting precipitation kinetics were calculated.

Results and discussion

Impact of plunge time during refill FSSW on the resulting microstructure

The three welded samples with varying plunge times were analyzed with 2D SAXS mapping and Fig. 5 shows the volume fraction distribution of size distribution 1, describing η-precipitates. In the base material, the highest volume fraction is measured. In the HAZ,

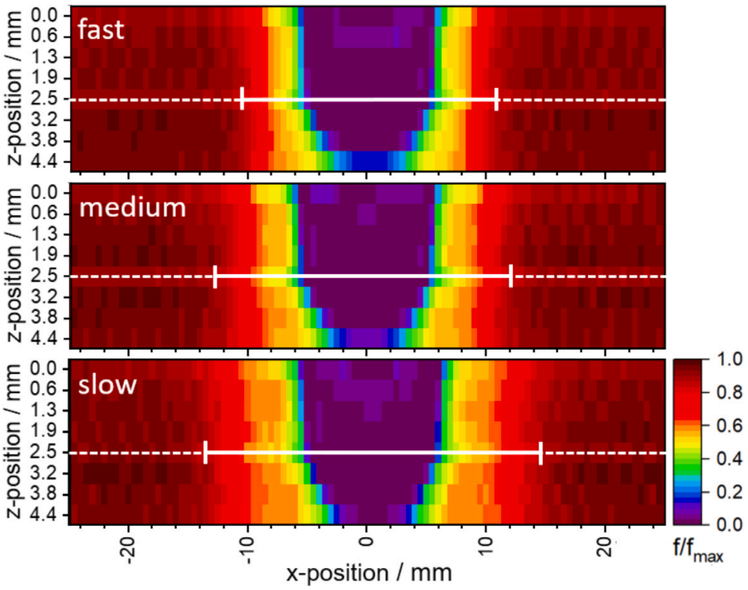

Fig. 5. 2D maps showing the distribution of volume fraction of η-precipitates (distribution 1) after refill FSSW in AA7050 with a variation of plunge times. The white lines represent the width of the welding zones. Line scans at z = 2.5 mm, represented by dashed white lines, are shown in Fig. 6.

the precipitates dissolve and the volume fraction decreases. In the SZ/TMAZ, the precipitates are almost completely dissolved. Comparing the three samples, differences are seen in the width and also the height of the welding zones for different plunging speeds. While precipitates are nearly completely dissolved under the welded spot at x = 0 mm and z = 4.4 mm in the slow welding process, small amounts are left after the fast welding process at these positions.

In Fig. 6, one line scan at z-position of 2.5 mm is shown. The volume fraction and mean radius distribution of η-precipitates are depicted. The width of the HAZ is increasing with increasing plunge time. In the slow welding process, the volume fraction decreases in a zone of −13.5 to 14.5 mm, i.e. the HAZ comprises a diameter of 28 mm. In contrast, the sample of the fast welding process shows a 6.5 mm smaller HAZ compared to the slow process. In a zone of 10 mm, precipitates are almost completely dissolved in all samples, which is slightly broader than the shoulder size (9 mm diameter). The welding process also influences the mean radius. In the base material, the precipitates have a size of 6.5 nm, whereas the HAZ shows an increase in mean radius and a maximum radius above 25 nm is measured at the edges of the SZ/TMAZ. Hence, coarsening of the remaining precipitates is seen in the weld zones. However, compared to precipitate dissolution a smaller zone is affected by particle growth. While dissolution is seen over the whole HAZ in the slow process, a precipitate size above 8 nm is only seen in a zone of 19 mm diameter. Therefore, dissolution happens already at lower temperatures in the outer zone of the HAZ.

While the precipitates with mean radii around 6.5 nm, which were present in the base material, are almost completely dissolved, a second size distribution of small precipitates with radii around 1–2 nm emerges in the SZ/TMAZ, which is exemplarily shown for the slow welding process in Fig. 7, but the same effect is seen after the fast and medium welding process as well. They are evenly distributed in the zone where η-precipitates were dissolved during the welding process. Those precipitates are presumably GP zones, which form through natural aging.

The thermo-mechanical cycle during refill FSSW is responsible for the microstructural changes. Due to the stirring it is difficult to get precise information about the temperature evolution in the SZ. But several experimental studies reported maximum temperatures above 500 °C in the SZ in AA7075 during refill FSSW, e.g. 540 °C (Reimann et al., 2017) or 501 °C at the boundary of the nugget (Shen et al., 2015), where (Zhao et al., 2016) obtained 530 °C in Alclad 7B04-T74, an alloy developed from AA7075. The reported temperatures significantly exceed dissolution temperatures of η'+η-precipitates (Kamp et al., 2009; Bush et al., 2024) and thus, a complete dissolution of precipitates is expected.

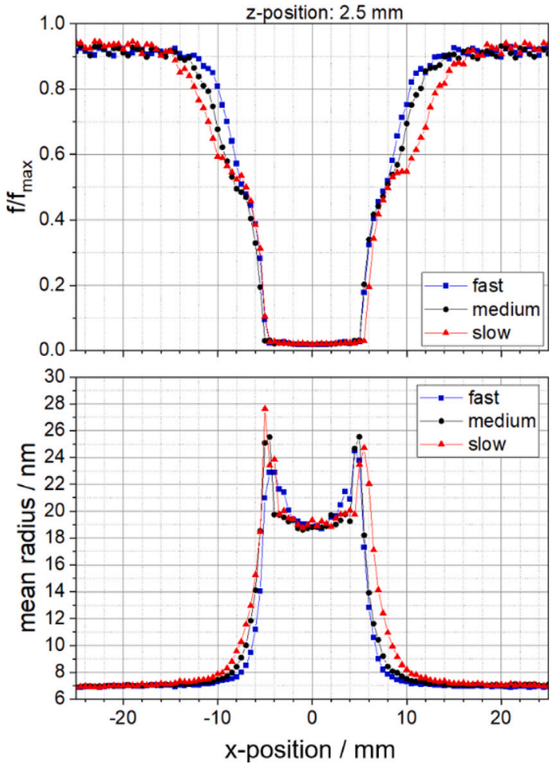

Fig. 6. Volume fraction and mean radius evolution of η-precipitates (distribution 1) measured in a line scan at a z-position of 2.5 mm.

Precipitation kinetics are largely governed by the maximum temperature, but also heating and cooling rates have a significant influence. Kamp et al. (2009) modeled kinetics during FSW in AA7050-T7451 and they considered both η and η'-precipitates in their model.

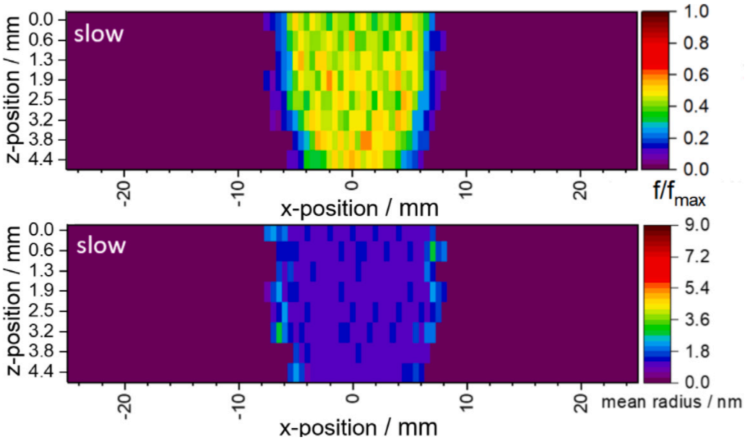

Fig. 7. 2D maps of the volume fraction and mean radius distribution of GP zones (distribution 2) after the slow welding process.

With peak temperatures between 300–340 °C, e.g. found in the HAZ, dissolution of small η'-precipitates is expected during heating. Larger η'-precipitates transform into η-phase. Small η dissolve as well with increasing temperature, while larger η-precipitates coarsen. The precipitates are predicted to completely dissolve at maximum temperatures above 400 °C according to their model. With increasing heating rates, as seen during higher welding speeds, more dissolution is expected as there is not enough time for coarsening of precipitates. Dissolution temperatures of precipitates were also reported by Bush et al. (2024), who conducted FSW and differential scanning calorimetry (DSC) on AA7050. At 170 °C, the smallest η'-precipitates started to dissolve. At 220–230 °C, η' further coarsened and transformation to η began. Large amounts of η dissolved at 320–330 °C and complete dissolution of all precipitates was seen at 430 °C. This shows that the elevated temperatures measured in the HAZ lead to dissolution and coarsening of precipitates. In the SZ/TMAZ, complete dissolution of precipitates is expected and hence, the solute concentration in the matrix is high in that zone. During cooling after the welding small amounts of coarse η might reprecipitate, as observed in this work, see Fig. 6.

Due to the high solute concentration through the dissolution of precipitates, natural aging occurs and was observed in many FSW and refill FSSW 7xxx samples (Reimann et al., 2017; Fuller et al., 2010; Su et al., 2003). The high solute concentration enables the formation of GP zones, which lead to a hardening effect (Fuller et al., 2010). The volume fraction of formed GP zones depends on the amount of available solute (Kamp et al., 2009), but also on aging time. An increase in hardness was seen in the SZ as well as the HAZ up to 4 weeks in AA7075 by Reimann et al. (2017). Fuller et al. (2010) studied the effect of natural aging in AA7050-T7651 and AA7075-T651 after FSW for a duration of 73,300 h and they measured a hardness increase through natural aging over a long period of time throughout all welding zones. Via transmission electron microscopy (TEM), they found precipitates with a size below 5 nm in a high density and larger precipitates with a size of 50 nm. They assigned the hardness increase between 48 and 216 h after welding to an increase in GP(I) zones. With further aging, some of these zones were substituted by GP(II) zones and small amounts of η'. Thus, the formation of GP zones through natural aging in the SZ/TMAZ is expected in this work, leading to a hardness increase.

Dumont et al. (2006) studied the precipitate distribution in AA7449 after FSW via TEM and SAXS. Similar to our work, 2D maps of the welding cross-sections were obtained with SAXS. In the SZ of a AA7449-T79 sample, the η-precipitates were also completely dissolved and GP zones with a size of 0.9 nm and a volume fraction of 4% were measured. In the outer TMAZ, no GP zones were found as large amounts of precipitates were not dissolved during welding, which then prevented the nucleation of GP zones. Additionally, they studied the influence of welding speed during FSW. With decreasing welding speed, the heat input became larger. This led to broader welding zones, as the time at higher temperature was longer and the zone, where temperatures above 150 °C were reached, was wider. These effects are also seen in this work, see Fig. 3. In the slow process, the maximum temperature as well as duration at high temperatures is higher at all positions, which leads to a broader HAZ through more energy input during the welding process. Additionally, the temperature field model by Zhao et al. (2016) for their refill FSSW process predicted higher temperatures near the bottom of the shoulder than near the outer edge of the shoulder. This might explain the dissolution of precipitates at the bottom of the samples although the plunge depth was only 2.6 mm in the welded samples in this work.

Nicolas and Deschamps (Nicolas and Deschamps, 2004) studied the HAZ of a metal inert gas-welded AA7108 alloy. Similar to our results, they had a transition zone where dissolution and coarsening of precipitates was seen. Coarsening was seen only in the zone with the highest peak temperatures, while dissolution happened in a broader zone. This effect can be explained by the critical radius. As temperature increases, the critical radius increases as well and is larger than all present precipitates. Hence, all particles get unstable and start to shrink and dissolve. Especially the small particles are affected as they have the highest dissolution rate, leading to a balanced mean radius. With increasing peak temperature and duration at elevated temperatures, the critical radius decreases due to the increasing solute concentration through dissolution, which enables the coarsening of larger particles. This explains the dissolution of precipitates in a broader zone in the HAZ and coarsening only close to the SZ as observed in this work.

The analysis of these samples shows the complex connection between welding parameters, energy input and resulting microstructure. Precipitation kinetics are largely influenced by peak temperatures and duration at elevated temperatures, which lead to dissolution, growth and coarsening of precipitates and hence, deterioration of mechanical properties. Natural aging due to a high solute concentration may lead to an enhancement in the SZ/TMAZ.

Modeling of precipitation kinetics in the HAZ with dilatometer

The temperature curves measured in the HAZ during the three different welding conditions at x-positions of 6.5 mm, i.e. underneath the clamping ring, and 11.5 mm, i.e. outside the region in contact with the welding tool, were simulated with the dilatometer and the corresponding SAXS results are shown in Figs. 8 and 9. At 11.5 mm, maximum temperatures of 200–240 °C are measured and it can be seen that these temperatures have no influence on the mean radius, but a small decrease in volume fraction is observed. At 6.5 mm, the peak temperatures are higher with 275–310 °C, but again, only a slight increase in mean radius from 6.4 to 8 nm is observed. In contrast,

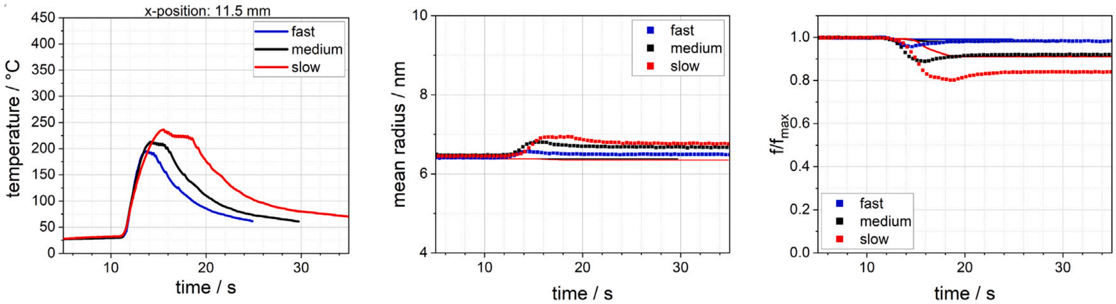

(a) (b) (c)

Fig. 8. (a) Temperature curves measured during refill FSSW at a height of z = 4.7 mm and x = 11.5 mm were simulated with the dilatometer. (b) Mean radius and (c) volume fraction evolution of η-precipitates were measured in-situ (squares) and modeled via PanPrecipitation (straight line).

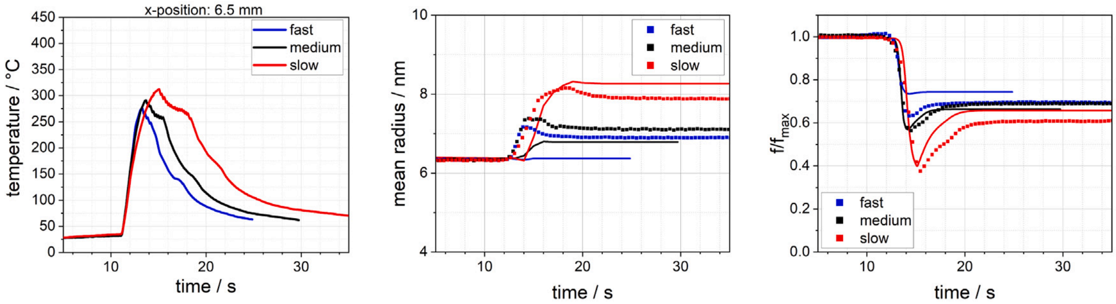

(a) (b) (c)

Fig. 9. (a) Temperature curves measured during refill FSSW at a height of z = 4.7 mm and x = 6.5 mm were simulated with the dilatometer. (b) Mean radius and (c) volume fraction evolution of η-precipitates were measured in-situ (squares) and modeled via PanPrecipitation (straight line).

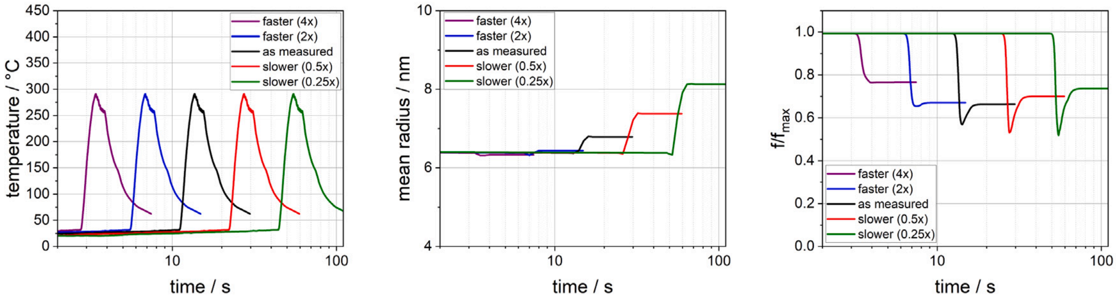

(a) (b) (c)

Fig. 10. (a) Influence of faster and slower plunge times was numerically determined by the Pandat model. Predicted evolutions of (b) mean radius and (c) volume fraction of η-precipitates are shown.

volume fractions drops to a minimum value and increases subsequently again. The temperature curves were used as input for our precipitation evolution model in Pandat, which can successfully predict the measured kinetics of η-precipitates, see Figs. 8 and 9. Similar to the ex-situ measurements described above, it can be seen that the volume fraction is strongly affected by the elevated temperatures. Although only slight coarsening is seen, large amounts of precipitates are dissolved at these temperatures.

Based on these results, predictions for faster and slower plunging speeds during refill FSSW were numerically determined. The measured temperature at 6.5 mm during medium welding speed was used as master curve with a maximum temperature of 290 ℃. Both faster and slower plunging speeds were mimicked, and the predicted mean radius and volume fraction evolution of η-precipitates are shown in Fig. 10.

During the faster weldings processes, mean radii stay constant at 6.4 nm, whereas a slower welding process leads to a particle growth to 8 nm. The volume fraction is predicted to decrease during all simulations, but differences in the final volume fraction and minima can be seen. During the 2x and 4x faster welding process, no distinct minimum appears. Only at longer plunge times, volume fraction drops to a clear minimum and increases again. Since the peak temperature is the same in all simulations, the differences are due to the different times at elevated temperatures. During the fastest simulated welding process, the temperature exceeds 250 °C for only 0.69 s. In contrast, the time above this temperature during the slowest welding is 11.1 s. Hence, there is much more time for diffusion processes, leading to precipitate dissolution and growth of remaining η-particles.

Post-weld heat treatments

As shown above, natural aging leads to the formation of GP zones in the SZ/TMAZ, responsible for hardness recovery. However, natural aging is time consuming and hence, impractical for industrial applications. Additionally, formation of GP zones through natural aging is only seen in a zone where enough solute is provided through previous dissolution of η-precipitates (Nicolas and Deschamps, 2004). This can

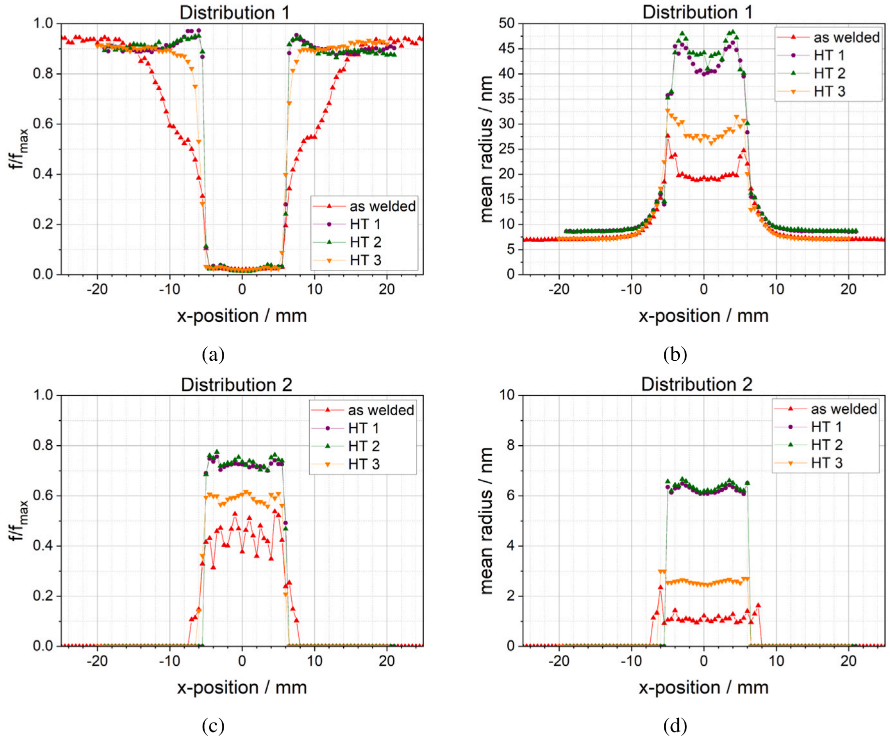

Fig. 11. Influence of conducted PWHT on (a) volume fraction and (b) mean radius of η-precipitates (distribution 1) and on the second size distribution (c+d). Shown is the influence on samples processed at slow welding conditions in line scans measured at z = 2.4 mm.

be prevented through artificial aging treatments after welding. The effect of different PWHT, see Table 2, was analyzed. As the broadest HAZ was seen in the sample processed at the lowest plunging speed, effects of PWHT are shown for this sample in Fig. 11, but the same effects occurred in all samples.

In the as-welded state, dissolution of η-precipitates in the HAZ is clearly visible. After the application of all PWHT, an increase in volume fraction in the HAZ is observed, which is comparable to the volume fraction in the base material. HT 1 and HT 2 with maximum temperatures of 163 °C lead to the same effect with maximum volume fractions measured next to the SZ/TMAZ. After HT 3 with a maximum temperature of 120 °C, the volume fraction decreases slightly in that zone. In the SZ/TMAZ, the remaining precipitates further coarsen with maximum radii of 50 nm after HT 1 and HT 2. A small increase in mean radii is also seen in the base material after these heat treatments. After HT 3, the mean radius in the base material stays constant, but slight coarsening happens in the SZ/TMAZ. After welding, also the second size distribution, which is assigned to GP zones, is measured. The application of PWHT increases the volume fraction and mean radii of this second distribution and presumably phase transformations are happening. While the GP zones have a size of around 1.5 nm in the as-welded state, a mean radius of 2.5 nm is measured after HT 3 and sizes of 6.5 nm after HT 1 and HT 2. According to these SAXS results, HT 1 and HT 2 lead to very similar results and no clear impact of the two-step aging treatment, which was conducted in HT 1, is seen.

The heat treatment at 163 °C was additionally applied for different durations, i.e. HT 4, and the influence on the volume fraction of size distribution 1 is shown in Fig. 12. In the as-welded state, the volume fraction of η-precipitates declines in the HAZ. The reduction in volume fraction is highest close to the SZ. Already after 20 min at 163 °C, an increase in volume fraction is clearly visible all over the HAZ, reaching nearly the maximum volume fraction, while only slight precipitate growth is observed. With prolonged time at this temperature, only small changes can be seen with a further increase in volume fraction close to the SZ.

Hardness measurements were conducted for the as-welded state and several heat-treated samples, see Fig. 13. The base material has a hardness of approximately 170 HV. The refill FSSW welding process leads to a reduction in hardness to values of around 150 HV in the SZ and a minimum of 130 HV in the TMAZ/HAZ. A reduction in hardness is observed in a zone of up to 12–14 mm distance along the radial direction. This corresponds with the SAXS results, in which precipitate dissolution was observed up to a distance of 14 mm along the radial direction. As the process leads to symmetric welds, a total width of up to 28 mm is affected by the welding process. It can be seen that all PWHT lead to an increase of hardness in the SZ, with values reaching 170–190 HV, which are equal to or even higher than those in the base material. For PWHT conducted for 20 min at 163 °C and 24 h at 120 °C, the hardness values observed in the outer areas of the HAZ also suggest that this region of material may have undergone recovery. In contrast, the treatment at 163 °C for 9 h presents a hardness decrease not only in the TMAZ/HAZ, but also in the base material, suggesting that the PWHT conditions led to overaging of the material. These results show that long aging times at low temperatures (24 h at 120 °C) and short aging times at higher temperatures (20 min at 163 °C) lead to similar results with an increase in hardness in the SZ and in the outer areas of the HAZ, where only dissolution of precipitates occurred. However, in that zone of the TMAZ/HAZ, where precipitates coarsened during welding, a hardness minimum remains after all PWHT and hardness could not be recovered without a solution treatment after welding.

Fig. 14 shows the resulting microstructure of the joints under the as-welded and heat-treated conditions, i.e. HT 3 (120 °C for 24 h) and HT 4 (163 °C for 20 min and 9 h). The macrographs highlight the SZ and TMAZ, which are characterized by the fine and equiaxed microstructure at the center of the weld (SZ) surrounded by the deformed grains of the TMAZ. The comparison of the weld zones across the samples indicates that the applied PWHT did not result in significant changes in the shape or size of these zones, considering the specific time–temperature combinations used in the investigation. Moreover, the observation of the macrographs alone does not indicate any changes

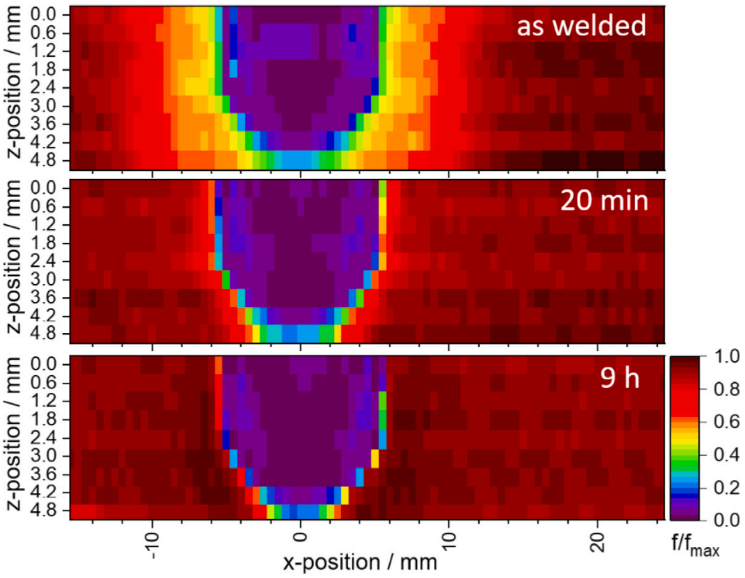

Fig. 12. 2D maps of the volume fraction of η-precipitates (distribution 1) in samples processed at slow plunging times after welding and after heat treatment HT 4 after two different heat treatment times, 20 min and 9 h, at 163 °C.

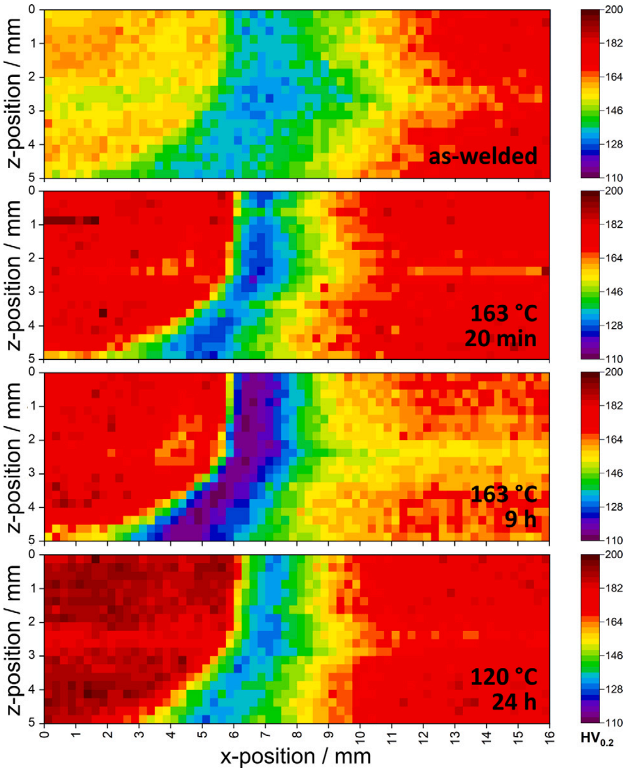

Fig. 13. Hardness maps of refill FSSW samples processed at slow plunging times: as-welded, and after HT 4 (163 °C for 20 min and 9 h) and HT 3 (120 °C for 24 h).

in the HAZ across the samples or in comparison to the base material, as no microstructural changes in terms of grain structure, such as grain growth, can be observed resulting from the conditions used in each PWHT.

In addition to the macrostructural identification of the weld zones across the samples, high magnification observations of the SZ and TMAZ show similar microstructural features resulting from the PWHT conditions. The analysis of the SZ microstructure at higher magnification, Fig. 14, indicates no evidence of further metallurgical transformations resulting from the thermodynamic and kinetic conditions associated with each PWHT, such as grain growth or static recrystallization. This is supported by the measured average grain sizes (d), which are consistent across the samples, varying less than 5 % around $\overline{d}$. Furthermore, high-magnification micrographs of the TMAZ presented in Fig. 14 show that the microstructure remains unchanged across the analyzed welds. This is an indication that, similarly to the other weld zones previously discussed, the PWHT does not induce metallurgical transformations, despite the severely deformed grains and consequently higher dislocation density characteristic of this region (Yuk et al., 2025), which typically favors mechanisms such as static recrystallization. These observations align with literature reports (Sun et al., 2019), which indicate that the critical temperature for grain growth and static recrystallization for AA7050 lies in the range of 450–500 °C.

In a temperature range between 330 and 430 °C, which occurs in the HAZ during refill FSSW, small η'-precipitates get dissolved. Coarse η' can transform into η, which is then also dissolved in large amounts. Thus, relatively large amounts of solute are left in the HAZ through the dissolution, which then enable reprecipitation during PWHT (Kamp et al., 2007). If the solute concentration is high enough, nucleation of new precipitates is possible. But when the solute content is too low for nucleation, only coarsening takes place (Nicolas and Deschamps, 2004). Compared to FSW, maximum temperatures as well as heating and cooling rates are higher during refill FSSW. This may lead to a high solute concentration over a wide range of the HAZ and therefore, reprecipitation is seen in this zone during PWHT. In the work of Nicolas and Deschamps (Nicolas and Deschamps, 2004), a hardness recovery could be achieved through reprecipitation in the zone where only dissolution of precipitates happened. In contrast, in the zone, where both coarsening and dissolution was seen, the hardness remained at minimum after PWHT as the coarsening seems to be the detrimental factor for the mechanical properties. This corresponds to the results observed in this work as a hardness minimum remained in the TMAZ/HAZ region after all conducted PWHT, while hardness increased in the SZ and outer areas of the HAZ.

During the heat treatments, phase transformations are expected. GP zones are stable at room temperature and may form up to 100 °C (Gupta et al., 2022) or 125 °C (Wang et al., 2024). GP zones can act as precursors to the formation of η'-phase or preferred nucleation sites

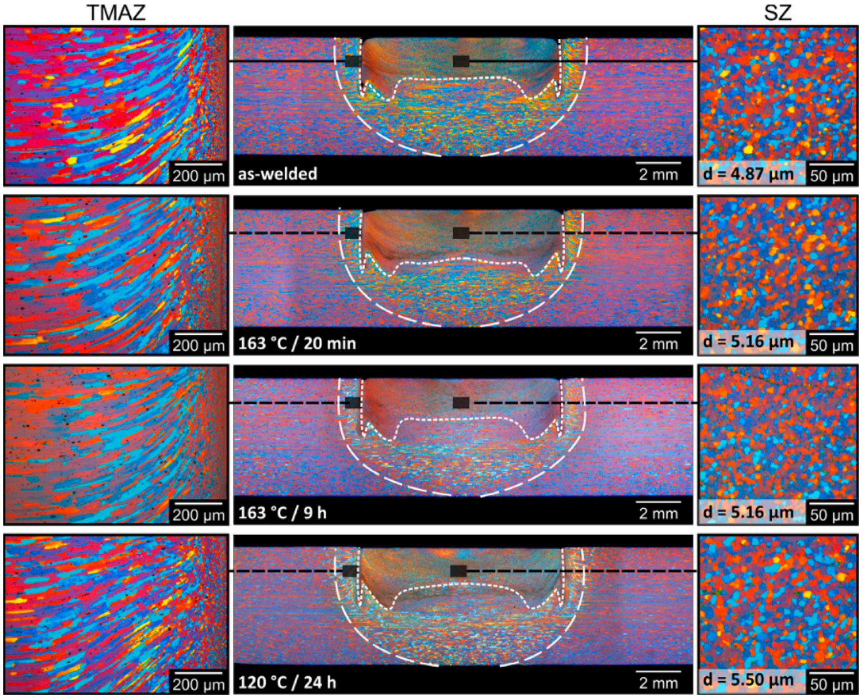

Fig. 14. Macrographs of refill FSSW samples processed at slow plunging times: as-welded, and after HT 4 (163 °C for 20 min and 9 h) and HT 3 (120 °C for 24 h), with detail to the SZ and TMAZ. White short- and long-dashed lines represent the limits of the SZ and TMAZ, respectively. *d* is the measured average grain size.

for the formation of η' (Azarniya et al., 2019). During temperatures of 120 °C, GP zones start to dissolve and η' can nucleate on these dissolving zones (Dumont et al., 2003). η' can also directly nucleate at elevated temperatures of 120–180 °C (Gupta et al., 2022), but the transformation based on GP zones is considered the main formation mechanism of η' (Wang et al., 2024). The transformation mechanism from η' to η is also not entirely known, but η starts to form at temperatures of 180 °C or elongated aging times at lower temperatures (Gupta et al., 2022). η'-particles could grow to their optimum size before a gradual substitution by η-precipitates takes place (Dumont et al., 2003). Kverneland et al. (2011) discussed a transformation to η when precipitates reach a maximum thickness of 3–4 nm, but also heterogeneous nucleation of η on grain boundaries or dislocations is possible. This phase transformation has to be considered as well in the modeling of precipitation kinetics in AA7xxx alloys. In the model of Kamp et al. (2007, 2009, 2006), the transformation of η' to η happened when a critical radius at a given temperature was reached. As an approximation, a transition radius of 6 nm was assumed at 150 °C, which decreased with increasing temperature (Kamp et al., 2006).

Based on literature, it can be assumed that GP zones are present in the SZ/TMAZ in the as-welded state in our samples. During HT 3 at 120 °C, GP zones may act as nucleation sites for the formation of η'. After HT 3, the mean radius stays below 3 nm and as the sample was artificially aged for 24 h, a microstructure containing mainly η' is assumed. In contrast, after HT 1 and HT 2 with peak temperatures of 163 °C, precipitates reach a mean radius above 6 nm and therefore, a phase transformation to mainly η-precipitates is expected.

Conclusions

High-energy small-angle X-ray scattering (SAXS) and precipitation modeling reveal the development of the spatial distribution of precipitates in AA7050 during the refill friction stir spot welding process. From this work, following conclusions can be drawn:

1. SAXS mapping shows the effect of plunging speed variations. Slower welding processes lead to a higher energy input, which results in a wider heat-affected zone (HAZ).
2. More dissolution of precipitates as well as growth and coarsening is seen in the HAZ with increasing peak temperatures. Complete dissolution of precipitates occurs in the stir zone (SZ). Natural aging leads to the nucleation of GP zones in the SZ and thermo-mechanically affected zone (TMAZ).
3. The employed precipitation model in Pandat can predict dissolution and growth of η-precipitates at elevated temperatures in the HAZ.
4. High peak temperatures as well as high heating and cooling rates lead to precipitate dissolution and hence, a high solute content in the SZ/TMAZ and HAZ after welding. The application of PWHT leads to reprecipitation already after short heat treatment durations in the HAZ. GP zones are transformed to η+η'-precipitates in the SZ/TMAZ during PWHT.
5. All conducted PWHT lead to an increase in hardness in the SZ and outer areas of the HAZ. Already 20 min at 163 °C resulted in strong reprecipitation. However, a hardness minimum remained in the TMAZ/HAZ, where precipitates coarsened during welding.
6. No significant changes are observed in the shape or size of the weld zones and their corresponding microstructures under the as-welded and the selected PWHT joints. This suggests that the applied time–temperature conditions do not induce metallurgical transformations such as grain growth or static recrystallization.

CRediT authorship contribution statement

Susanne Henninger: Writing – original draft, Visualization, Investigation, Formal analysis. **Rupesh Chafle:** Software, Investigation, Formal analysis, Writing – original draft. **Niklaas Becker:** Methodology, Investigation, Writing – review & editing. **Camila C. de Castro:** Investigation, Visualization, Writing – review & editing. **Benjamin**

Klusemann: Writing – review & editing, Supervision, Project administration. **Martin Müller:** Supervision. **Peter Staron:** Writing – review & editing, Supervision, Project administration.

Declaration of competing interest

The authors declare that they have no known competing financial interests or personal relationships that could have appeared to influence the work reported in this paper.

Acknowledgments

We acknowledge DESY (Hamburg, Germany), a member of the Helmholtz Association HGF, for the provision of the experimental facilities. Parts of this research were carried out at PETRA III. Data was collected using the High Energy Materials Science beamline P07 operated by Helmholtz-Zentrum Hereon.

Data availability

Data will be made available on request.

References

Airbus, 2024. Global market forecast 2024–2043.

Azarniya, A., Taheri, A., Taheri, K., 2019. Recent advances in ageing of 7xxx series aluminum alloys: A physical metallurgy perspective. J. Alloys Compd. 781, 945–983.

Barbini, A., Carstensen, J., dos Santos, J., 2018. Influence of alloys position, rolling and welding directions on properties of AA2024/AA7050 dissimilar butt weld obtained by friction stir welding. Metals 8 (4), 202.

Becker, N., dos Santos, J., Klusemann, B., 2024. Experimental investigation of crack propagation mechanism in refill friction stir spot joints of AA6082-T6. Eng. Fract. Mech. 300, 109963.

Boeing, 2024. Commercial market outlook 2024–2043.

Bush, R., Feier, I., Diercks, D., 2024. Precipitate structure, microstructure evolution modeling and characterization in an aluminum alloy 7050 friction stir weld. J. Mater. Eng. Perform.

Cao, W., Chen, S.-L., Zhang, F., Wu, K., Yang, Y., Chang, Y., Schmid-Fetzer, R., Oates, W., 2009. PANDAT software with PanEngine, PanOptimizer and PanPrecipitation for multi-component phase diagram calculation and materials property simulation. Calphad 33 (2), 328–342.

Cao, F., Zheng, J., Jiang, Y., Chen, B., Wang, Y., Hu, T., 2019. Experimental and DFT characterization of η' nano-phase and its interfaces in Al-Zn-Mg-Cu alloys. Acta Mater. 164, 207–219.

CompuTherm LLC, 2021. PANDAT™2021 user's guide.

CompuTherm LLC, 2025. Introducing pandat software - an integrated modeling platform for materials design. https://computherm.com/. (Accessed 28 May 2025).

De Geuser, F., Deschamps, A., 2012. Precipitate characterisation in metallic systems by small-angle X-ray or neutron scattering. Comptes Rendus Phys. 13 (3), 246–256.

Dong, J., Zhang, D., Zhang, W., Cao, G., Qiu, C., 2023. Effect of post-weld heat treatments on the microstructure and mechanical properties of underwater friction stir welded joints of 7003-T4/6060-T4 aluminium alloys. Mater. Sci. Eng. A 862, 144423.

Dumont, D., Deschamps, A., Brechet, Y., 2003. On the relationship between microstructure, strength and toughness in AA7050 aluminum alloy. Mater. Sci. Eng. A 356 (1–2), 326–336.

Dumont, M., Steuwer, A., Deschamps, A., Peel, M., Withers, P., 2006. Microstructure mapping in friction stir welds of 7449 aluminium alloy using SAXS. Acta Mater. 54 (18), 4793–4801.

Dursun, T., Soutis, C., 2014. Recent developments in advanced aircraft aluminium alloys. Mater. Des. 56, 862–871.

European Committee for Standardization - E.N. 573-3, 2024. Aluminium and aluminium alloys - chemical composition and form of wrought products - part 3: Chemical composition and form of products.

Fribourg, G., Deschamps, A., Bréchet, Y., Mylonas, G., Labeas, G., Heckenberger, U., Perez, M., 2011. Microstructure modifications induced by a laser surface treatment in an AA7449 aluminium alloy. Mater. Sci. Eng. A 528 (6), 2736–2747.

Fuller, C., Mahoney, M., Calabrese, M., Micona, L., 2010. Evolution of microstructure and mechanical properties in naturally aged 7050 and 7075 Al friction stir welds. Mater. Sci. Eng. A 527 (9), 2233–2240.

Gao, X., Gao, G., Li, Z., Li, X., Yan, L., Zhang, Y., Xiong, B., 2024. Effects of different heating and cooling rates during solution treatment on microstructure and properties of AA7050 alloy wires. Materials 17 (2), 310.

Guo, Y., He, X., Liu, C., Wei, C., Yang, R., Dong, X., 2023. Study on the effects of ultrasonic assistance and external heat dissipation on friction stir welded 7075 aluminum alloy joints. J. Manuf. Process. 107, 280–293.

Gupta, S., Haridas, R., Agrawal, P., Mishra, R., Doherty, K., 2022. Influence of welding parameters on mechanical, microstructure, and corrosion behavior of friction stir welded Al 7017 alloy. Mater. Sci. Eng. A 846, 143303.

Habba, M., Ahmed, M., 2025. Friction stir welding of dissimilar aluminum and copper alloys: A review of strategies for enhancing joint quality. J. Adv. Join. Process. 11, 100293.

Heidarzadeh, A., Mironov, S., Kaibyshev, R., Çam, G., Simar, A., Gerlich, A., Khodabakhshi, F., Mostafaei, A., Field, D., Robson, J., Deschamps, A., Withers, P., 2021. Friction stir welding/processing of metals and alloys: A comprehensive review on microstructural evolution. Prog. Mater. Sci. 117, 100752.

Henninger, S., Chafle, R., Maawad, E., Klusemann, B., Müller, M., Staron, P., 2025. Impact of friction stir welding-like heat cycles on precipitates in AA7050 analysed by SAXS and numerical modelling. Materialia 39, 102343.

Huang, E.-W., Liaw, P., Porcar, L., Liu, Y., Liu, Y.-L., Kai, J.-J., Chen, W.-R., 2008. Study of nanoprecipitates in a nickel-based superalloy using small-angle neutron scattering and transmission electron microscopy. Appl. Phys. Lett. 93, 161904.

Ilavsky, J., 2012. Nika: software for two-dimensional data reduction. J. Appl. Crystallogr. 45, 324–328.

Ilavsky, J., Jemian, P., 2009. Irena: tool suite for modeling and analysis of small-angle scattering. J. Appl. Crystallogr. 42, 347–353.

Jacumasso, S., Martins, J., Carvalho, A., 2016. Analysis of precipitate density of an aluminium alloy by TEM and AFM. REM: Int. Eng. J. 69 (4), 451–457.

Janga, V., Awang, M., Sallih, N., Lemma, T., 2025. Thermo-mechanical and material flow characteristics of tool sequencing dynamics in refill FSSW of thin alclad AA7075-T6 sheets: Numerical analysis using meshless smoothed-particle hydrodynamics methods. J. Adv. Join. Process. 11, 100285.

Kammerer, C., Behdad, S., Zhou, L., Betancor, F., Gonzalez, M., Boesl, B., Sohn, Y., 2015. Diffusion kinetics, mechanical properties, and crystallographic characterization of intermetallic compounds in the Mg-Zn binary system. Intermetallics 67, 145–155.

Kamp, N., Reynolds, A., Robson, J., 2009. Modelling of 7050 aluminium alloy friction stir welding. Sci. Technol. Weld. Join. 14 (7), 589–596.

Kamp, N., Sullivan, A., Robson, J., 2007. Modelling of friction stir welding of 7xxx aluminium alloys. Mater. Sci. Eng. A 466 (1–2), 246–255.

Kamp, N., Sullivan, A., Tomasi, R., Robson, J., 2006. Modelling of heterogeneous precipitate distribution evolution during friction stir welding process. Acta Mater. 54 (8), 2003–2014.

Kumar, P., Reddy, G., Rao, K., 2015. Microstructure, mechanical and corrosion behavior of high strength AA7075 aluminium alloy friction stir welds - effect of post weld heat treatment. Def. Technol. 11 (4), 362–369.

Kverneland, A., Hansen, V., Thorkildsen, G., Larsen, H., Pattison, P., Li, X., Gjønnes, J., 2011. Transformations and structures in the Al-Zn-Mg alloy system: A diffraction study using synchrotron radiation and electron precession. Mater. Sci. Eng. A 528 (3), 880–887.

Lezaack, M., Simar, A., 2021. Avoiding abnormal grain growth in thick 7XXX aluminium alloy friction stir welds during T6 post heat treatments. Mater. Sci. Eng. A 807, 140901.

Liu, D., Xiong, B., Bian, F., Li, Z., Li, X., Zhang, Y., Wang, F., Liu, H., 2013. Quantitative study of precipitates in an Al-Zn-Mg-Cu alloy aged with various typical tempers. Mater. Sci. Eng. A 588, 1–6.

Liu, D., Xiong, B., Bian, F., Li, Z., Li, X., Zhang, Y., Wang, Q., Xie, G., Wang, F., Liu, H., 2015. Quantitative study of nanoscale precipitates in Al-Zn-Mg-Cu alloys with different chemical compositions. Mater. Sci. Eng. A 639, 245–251.

Maji, P., Nath, R., Karmakar, R., Paul, P., Meitei, R., Ghosh, S., 2021. Effect of post processing heat treatment on friction stir welded/processed aluminum based alloys and composites. CIRP J. Manuf. Sci. Technol. 35, 96–105.

Marlaud, T., Deschamps, A., Bley, F., Lefebvre, W., Baroux, B., 2010a. Evolution of precipitate microstructures during the retrogression and re-ageing heat treatment of an Al-Zn-Mg-Cu alloy. Acta Mater. 58 (14), 4814–4826.

Marlaud, T., Deschamps, A., Bley, F., Lefebvre, W., Baroux, B., 2010b. Influence of alloy composition and heat treatment on precipitate composition in Al-Zn-Mg-Cu alloys. Acta Mater. 58 (1), 248–260.

Meng, X., Huang, Y., Cao, J., Shen, J., dos Santos, J., 2021. Recent progress on control strategies for inherent issues in friction stir welding. Prog. Mater. Sci. 115, 100706.

Nicolas, M., Deschamps, A., 2004. Precipitate microstructures and resulting properties of Al-Zn-Mg metal inert gas-weld heat-affected zones. Met. Mater. Trans. A 35, 1437–1448.

Rathinasuriyan, C., Pavithra, E., Sankar, R., Senthil Kumar, V., 2021. Current status and development of submerged friction stir welding: A review. Int. J. Precis. Eng. Manufacturing-Green Technol. 8, 687–701.

Raza, S., Mittnacht, T., Diyoke, G., Schneider, D., Nestler, B., Klusemann, B., 2022. Modeling of temperature- and strain-driven intermetallic compound evolution in an Al-Mg system via a multiphase-field approach with application to refill friction stir spot welding. J. Mech. Phys. Solids 169, 105059.

Reimann, M., Goebel, J., dos Santos, J., 2017. Microstructure and mechanical properties of keyhole repair welds in AA7075-T651 using refill friction stir spot welding. Mater. Des. 132, 283–294.

Reynolds, A., Tang, W., Khandkar, Z., Khan, J., Lindner, K., 2005. Relationships between weld parameters, hardness distribution and temperature history in alloy 7050 friction stir welds. Sci. Technol. Weld. Join. 10 (2), 190–199.

Shen, Z., Chen, Y., Hou, J., Yang, X., Gerlich, A., 2015. Influence of processing parameters on microstructure and mechanical performance of refill friction stir spot welded 7075-T6 aluminium alloy. Sci. Technol. Weld. Join. 20 (1), 48–57.

Shen, Z., Ding, Y., Gerlich, A., 2020. Advances in friction stir spot welding. Crit. Rev. Solid State Mater. Sci. 45 (6), 457–534.

Sivaraj, P., Kanagarajan, D., Balasubramanian, V., 2014. Effect of post weld heat treatment on tensile properties and microstructure characteristics of friction stir welded armour grade AA7075-T651 aluminium alloy. Def. Technol. 10 (1), 1–8.

Su, J.-Q., Nelson, T., Mishra, R., Mahoney, M., 2003. Microstructural investigation of friction stir welded 7050-t651 aluminium. Acta Mater. 51 (3), 713–729.

Sullivan, A., Robson, J., 2008. Microstructural properties of friction stir welded and post-weld heat-treated 7449 aluminium alloy thick plate. Mater. Sci. Eng. A 478 (1–2), 351–360.

Sun, Y., Bai, X., Klenosky, D., Trumble, K., Johnson, D., 2019. A study on peripheral grain structure evolution on an AA7050 aluminum alloy with a laboratory-scale extrusion setup. J. Mater. Eng. Perform. 28, 5156–5164.

Villars, P., 2023. $MgZn_2$ crystal structure (sd_0261233), pauling file. In: Materials, S. (Ed.), Inorganic Solid Phases, SpringerMaterials (online database). Springer, Heidelberg.

Wang, K., Naumov, A., Panchenko, E., Panchenko, O., 2024. A review on friction stir welding of high-strength Al-Zn-Mg alloy: Insights on second-phase particles. Materials 17 (20), 5107.

Wu, H., Chen, Y.-C., Strong, D., Prangnell, P., 2015. Stationary shoulder FSW for joining high strength aluminum alloys. J. Mater. Process. Technol. 221, 187–196.

Yuk, S., Shim, S., Jeong, M., Lee, D., Lee, K., Kim, S., Lee, S., Han, J., 2025. Micro/nanostructure evolution and deformation mechanisms in friction-stir-welded 7075 Al alloy: A comparative analysis of weld zones. J. Mater. Res. Technol. 36, 5193–5210.

Zhang, H., Wang, B., Li, G., Chang, W., Dong, D., 2022. Fatigue crack growth performance of refilled friction stir spot welds in similar and dissimilar aluminum alloy joints. In: Chinese Society of Aeronautics and Astronautics (Ed.), Proceedings of the 5th China Aeronautical Science and Technology Conference. Springer Nature Singapore Pte Ltd., pp. 209–219.

Zhao, Y., Liu, H., Yang, T., Lin, Z., Hu, Y., 2016. Study of temperature and material flow during friction spot welding of 7b04-T74 aluminum alloy. Int. J. Adv. Manuf. Technol. 83, 1467–1475.

Zhou, B., Liu, B., Zhang, S., 2021. The advancement of 7XXX series aluminum alloys for aircraft structures: A review. Metals 11 (5), 718.